The Aeronautical Journal (2026), **130**, pp. 1836–1858
doi:10.1017/aer.2026.10153

RESEARCH ARTICLE

A design method for single expansion ramp nozzle based on three-dimensional characteristic method

Zhao Zhang[1], Wenyan Song[1] and Zheng Zhou[2]

[1]Northwestern Polytechnical University, China
[2]China Aerodynamics Research and Development Center, China
Corresponding author: Wenyan Song; Email: wenyan_song@nwpu.edu.cn

Received: 23 April 2025; **Revised:** 25 February 2026; **Accepted:** 25 February 2026

Keywords: design of three-dimensional nozzle; three-dimension method of characteristics; tracing profile; single expansion ramp nozzle

Abstract

To enhance the aerodynamic performance of hypersonic nozzles, a three-dimensional method of characteristics (3D MOC) is proposed for designing single expansion ramp nozzles (SERN). The flowfield structures and aerodynamic performances of nozzles designed using the 3D and conventional two-dimensional (2D) MOC approaches are compared through three-dimensional numerical simulations. Results indicate that the major geometric differences occur along the circumferential wall. Under typical flight conditions, the nozzle designed by 3D MOC achieves over 0.45% higher axial thrust coefficient and more than 8% higher lift coefficient than the 2D MOC design. Furthermore, based on the 3D MOC, both rectangular nozzle (RN) and circular nozzle (CN) configurations are designed and analysed. The CN exhibits slightly superior aerodynamic performance compared with the RN. By further modifying the upper and lower wall infill surfaces of the RN, three new nozzle variants are obtained. Comparative results show that these geometric infills have a pronounced influence on lift and pitching moment, while the axial thrust coefficient remains nearly constant. Finally, the effect of the tracing radius on the RN and CN configurations is examined. Increasing the tracing radius notably reduces the lift coefficient but has minimal impact on the thrust and pitching moment. These findings highlight the potential of the 3D MOC-based design method to flexibly balance aerodynamic moment and lift in hypersonic nozzle optimisation.

Nomenclature

CN	circular nozzle
RN	rectangular nozzle
CFD	computational fluid dynamics
MOC	method of characteristics
SERN	single expansion ramp nozzles
TBCC	turbine-based combined cycle
CFL	ourant-Friedrichs-Lewy
RANS	eynolds-averaged Navier-Stokes
SST	shear-stress transport
a	speed of sound
A	projected area of the nozzle along the axial direction
C_{fx}	axial thrust coefficient
C_y	lift
F_{cx}	axial thrust
F_s	isentropic thrust
L_n	nozzle length
M	pitching moment

© The Author(s), 2026. Published by Cambridge University Press on behalf of Royal Aeronautical Society.

$\dot{m}$	mass flow rate
p	pressure
p_t	total pressure
q	velocity
R	gas constant
R_x	axial thrust
Re_x	local Reynolds number
T	temperature
T_t	total temperature
T^*	reference temperature
u	velocity along x direction
μ	viscosity
k	turbulence kinetic energy
ω	specific dissipation rate of turbulence
z	z direction coordinate
β	Mach angle
δ	parametric angle
δ_1	displacement thickness of boundary layer
θ	flow angle
v	velocity along y direction
w	velocity along z direction
x	X direction coordinate
y	Y direction coordinate
ψ	azimuthal angle
γ	specific heat ratio of gas
ρ	density
π	pressure drop ratio of the nozzle

Subscript

0	ambient
aw	adiabatic wall
pri	primary flow
w	wall
inx	entrance of the nozzle along the axial direction
l	laminar
t	turbulent
ref	reference

1.0 Introduction

Request for a fast global-reach capability has driven hypersonic technology, which generally refers to the vehicle that can fly in the atmosphere at high speed or even across the atmosphere after taking off from the ground, and has great application prospects in civil and military fields [1]. Needless to say, this has attracted widespread attention. Furthermore, its core technology is propulsion technology of the power system, which requires a wide flight Mach number range to ensure the aircraft can successfully complete the mission from subsonic, transonic, supersonic to hypersonic. Therefore, it is an inevitable choice to integrate a single propulsion system into a combined propulsion system. In the concept of the combined power propulsion system proposed so far, the turbine-based combined cycle (TBCC) with high safety, low operating cost and reusability can be used as an ideal engine for hypersonic vehicles. As one of the core components of TBCC, the exhaust system not only controls the working state of the engine, but also provides thrust for the aircraft at a high flight Mach number. Moreover, for the integration of the airframe/propulsion system of a hypersonic vehicle, the nozzle is usually fused with the forebody of aircraft, which forms a single expansion ramp nozzle (SERN) with an asymmetry, light

https://doi.org/10.1017/aer.2026.10153 Published online by Cambridge University Press

weight, simple structure and highly compensated functions. In particular, 70% of the net thrust of the propulsion systems provided by SERN at the flight Mach number beyond 6 [2], and a 1% decrease in the thrust coefficient of SERN will result in a reduction of 4% in the installation net thrust of the propulsion system [3]. Therefore, it is necessary to improve the design technique level of SERN, which directly affects the performance of the whole propulsion system.

As a traditional design method by applying the method of characteristics (MOC), Argrow [4] studies the flowfield and wall profile of the perfect nozzle, which has the uniform and parallel outflow with the desired Mach number to maximise the nozzle thrust. However, the nozzle length cannot be accurately controlled and is significantly beyond the expected range for the propulsion system, which is needed to decrease for integration design. Hence, new approaches are developed subsequently, especially the minimum length nozzle [5], which is mainly reflected in increasing the expansion rate of the initial expansion section [6]. In terms of SERN, Göing [7] was the first to develop the optimised SERN for hypersonic propulsion using the MOC. Besides, several design methods have been proposed to reduce the length of the nozzle without degrading performance. Hoffman [8] firstly proposed a method to generate the profile of the linearly compressed perfect nozzle, which has better performance and is considered as a good choice for a propulsion system. Quan et al. [9] proposed the design method of nonlinear compression that keeps the initial expansion section with large effort on the wall unchanged to ensure the performance, while the compression of the wall with less contribution on thrust was increased to meet the need of shortening length and reducing the weight of the nozzle. Furthermore, considering the relationship between thrust and friction drag on the internal wall, a new method for designing truncated perfect nozzle was proposed by analysing the force on the wall unit of nozzle [10]. Due to the relatively simple and effective truncation method, it is rapidly used for the design of the SERN in the early research.

Unlike the perfect nozzle, another classical design theory that applies the MOC-named maximum thrust nozzle was first proposed by Guderley and Hantsch [11],which can be designed by variational calculus under a certain nozzle length and ambient pressure. Subsequently, Rao [12] successfully applied a method of the Lagrange multiplier to obtain the nozzle with maximum thrust under the given nozzle length and mass flow, which is also called a Rao nozzle. On the basis of the maximum thrust nozzle, Lv et al. [13] proposed a novel design method to determine a 2D SERN with full geometric constraints directly, which significantly shortened the design time. The abovementioned design methods still have some disadvantages, such as a lack of flexibility in controlling the outlet shape. Thus, an inverse design method based on maximum thrust theory is proposed by Yu et al. [14, 15] in order to demonstrate additional flexibility under geometrical constraints and full integration with airframes. The flow parameters and the shape of the nozzle outlet can be specified in advance in accordance with the actual requirements. Chen et al. [16] and Lv et al. [17] also put forward a new design method by limiting the length and height constraints, whose geometric variables used for constraints are scale factors and asymmetry factors. Compared with the linearly compressed perfect nozzle, the SERN generated by the new method can not only meet the constraints of multiple geometric dimensions, but also significantly improve the performance of the nozzle at the same time. Based on maximum thrust theory, Li et al. [18] utilised the slip-line unit process to divide the flowfield of the nozzle into upper and lower parts to calculate separately, so as to reduce the negative effect of the internal discontinuity on aerodynamic performance.

In addition to the above-mentioned design method of 2D SERN, 3D SERN, which can better integrate with the round or elliptical combustor [19], has a higher expansion efficiency resulting from the lateral expansion. Thompson et al. [20] utilised variational method to optimise a 3D maximum thrust nozzle under specific geometric constraints initially. Following this method, Snyder et al. [21] further completed the design of the 3D non-axisymmetric nozzle with a maximum thrust theory under the given constraints of entry parameter, flow rate and outlet shape in 1971. With the development of the computer and computational fluid dynamics (CFD), the hybrid optimisation method was employed to obtain a quasi-axisymmetric 3D nozzle operating at Mach 7.9 [22]. However, due to the requirement of a large amount of calculation with full 3D simulation, the optimisation method cannot be widely applied to the design of nozzle. Therefore, thanks to the proposal and development of the streamline tracing method, the 3D SERN design mainly adopts this method at present, and the obtained nozzle inherited the same

https://doi.org/10.1017/aer.2026.10153 Published online by Cambridge University Press

inviscid flowfield characteristic from the parent flowfield [23, 24]. Lu et al. [25] initially developed the design method of 3D SERN by using a streamline tracing method based on the axisymmetric maximum thrust flowfield, and the thrust and lift of the resulting nozzle increased compared with the straight wall configuration. To overcome the shortcoming that the exit shape of the 3D SERN was uncontrollable for a given entry shape, Mo et al. [26] learned from the rectangular-to-elliptical shape transition method and blended two streamline-traced nozzles along both forward and reverse directions in an annular flowfield to obtain a 3D SERN. However, due to the negative contribution of the lower cowl, the 3D SERN designed by Mo always produced negative lift and small nose-down pitching moment. Consequently, Lv et al. [27] proposed a new method to design the 3D streamline-traced SERN that can be trimmed along the last characteristic line of the parent flowfield to improve the performance, and a small amount of axial thrust was lost, while the lift and pitching moment were greatly increased. Considering that the profile of the 3D SERN could be easily deformed by mixing streamlines tracing from the entry and exit of the nozzle, respectively, Hua et al. [28] put forward an osculating method which assumed that the flowfield of the 3D variable cross-section nozzle were composed of countless different 2D parent flowfields based on the maximum thrust theory, and all the tracked streamlines in the 2D parent flowfields were combined reasonably to form a 3D SERN. Kunze and Smart [29] proposed a design method for 3D SERN that allows for tailoring the shape of the nozzle to a variety of vehicles, which could employ streamline tracing to capture the properties of an axisymmetric parent flowfield with a central body based on the maximum thrust nozzle.

As stated above, the present study demonstrates that the airflow at the entry is swirling and will pass through the whole nozzle accompanied by the flow, so there are obvious 3D unsteady characteristics in the whole flowfield. However, most of the 3D nozzle design based on the parent flowfield based on 2D MOC inherits the characteristics of the 2D nozzle. Therefore, the design method of the 3D SERN should continue to be developed, such as the 3D MOC, and the key is to reduce the complexity of the 3D MOC design with reasonable assumptions and simplifications.

In this paper, a 3D SERN based on 3D MOC is designed by using the streamline tracing technique firstly; then the performance comparison of the designed 3D SERN based on 2D MOC and 3D MOC, respectively, is studied. After that, the design and comparative analysis of the rectangular and circular 3D SERN are completed when considering the influence of the tracing profile. Finally, the effect of the tracing radius on the performance of the 3D SERN is investigated.

2.0 Design of method

2.1 Three-dimensional method of characteristic

3D MOC [30] is developed on the basis of 2D MOC, which can calculate the three-dimensional flowfield characteristics under the given flowpath geometry and entry conditions. The reference plane method is used to solve the 3D MOC equations, which contain the characteristic equations and the compatibility equations. And the 3D MOC equation consists of the following equations.

2.1.1 Equation of motion

The steady, inviscid, 3D flow equations for an ideal gas are:

Continuity:

$$u\frac{\partial u}{\partial x}+v\frac{\partial u}{\partial y}+w\frac{\partial u}{\partial z}+\frac{1}{\rho}\frac{\partial p}{\partial x}=0 \tag{1}$$

Momentum:

$$u\frac{\partial u}{\partial x}+v\frac{\partial u}{\partial y}+w\frac{\partial u}{\partial z}+\frac{1}{\rho}\frac{\partial p}{\partial x}=0 \tag{2}$$

https://doi.org/10.1017/aer.2026.10153 Published online by Cambridge University Press

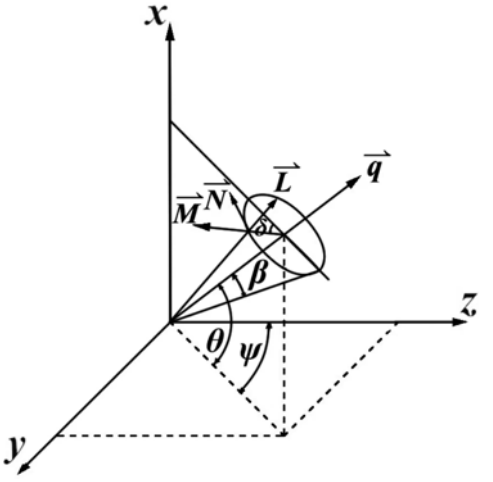


Figure 1. *Schematic of Mach conoid coordinate system based on 3D MOC.*

$$u\frac{\partial v}{\partial x}+v\frac{\partial v}{\partial y}+w\frac{\partial v}{\partial z}+\frac{1}{\rho}\frac{\partial p}{\partial y}=0 \tag{3}$$

$$u\frac{\partial w}{\partial x}+v\frac{\partial w}{\partial y}+w\frac{\partial w}{\partial z}+\frac{1}{\rho}\frac{\partial p}{\partial z}=0 \tag{4}$$

Energy:

$$u\frac{\partial h}{\partial x}+v\frac{\partial h}{\partial y}+w\frac{\partial h}{\partial z}+\frac{1}{\rho}\left(u\frac{\partial p}{\partial x}+v\frac{\partial p}{\partial y}+w\frac{\partial p}{\partial z}\right)=0 \tag{5}$$

State:

$$p=\rho RT \tag{6}$$

2.1.2 Characteristic equations

The equations of motion give rise to two sets of characteristic surfaces. The defined equations are:

$$(uf_x+vf_y+wf_z)^2=0 \tag{7}$$

and

$$(ug_x+vg_y+wg_z)^2-a^2\left(g_x^2+g_y^2+g_z^2\right)=0 \tag{8}$$

where a denotes the speed of sound, and $f\ (x, y, z)=0$ and $g\ (x, y, z)=0$ are the characteristic surfaces. The first surface is composed of streamlines and the second is the Mach conoid.

The flow Mach conoid is schematically shown in Fig. 1, in which $\boldsymbol{M}$, $\boldsymbol{N}$ and $\boldsymbol{L}$, respectively, represent the direction of the unit feature normal on the feature surface.

Where the equation of a ray, or bicharacteristic, of the Mach conoid may be expressed as

$$\mathrm{d}x=(\cos\beta\sin\theta+\sin\beta\cos\theta\cos\delta)\,\mathrm{d}L \tag{9}$$

$$\mathrm{d}y=[\cos\beta\cos\theta\sin\psi-\sin\beta\,(\sin\theta\sin\psi\cos\delta-\cos\psi\sin\delta)]\,\mathrm{d}L \tag{10}$$

$$\mathrm{d}z=[\cos\beta\cos\theta\cos\psi-\sin\beta\,(\sin\theta\cos\psi\cos\delta+\sin\psi\sin\delta)]\,\mathrm{d}L \tag{11}$$

where β is the Mach angle, $\mathrm{d}L$ is the distance along the bicharacteristic, δ is a parametric angle and θ and ψ are related to the velocity vector by

$$u=q\sin\theta \tag{12}$$

https://doi.org/10.1017/aer.2026.10153 Published online by Cambridge University Press

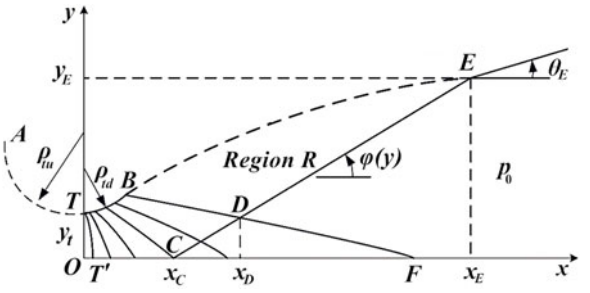


Figure 2. *Basic flowfield of axisymmetric maximum thrust nozzle.*

$$v = q\cos\theta\sin\psi \tag{13}$$

$$w = q\cos\theta\cos\psi \tag{14}$$

2.1.3 Compatibility equations

The compatibility equations are determined by the flow equations and the requirement that the derivatives in a direction normal to the characteristic surface disappear. The compatibility equation, which applies along the Mach conoid, is

$$\frac{\cot\beta}{\rho q^2}\frac{\partial p}{\partial L} + \cos\delta\frac{\partial\theta}{\partial L} + \cos\theta\sin\delta\frac{\partial\psi}{\partial L} + \sin\beta\left(\cos\theta\cos\delta\frac{\partial\psi}{\partial N} - \sin\delta\frac{\partial\theta}{\partial N}\right) = 0 \tag{15}$$

where $\frac{\partial}{\partial L}$ and $\frac{\partial}{\partial N}$ are derivatives along and normal to the bicharacteristic.

The compatibility equations along a streamline are

$$\frac{\gamma}{\gamma-1}R\mathrm{d}T = \frac{1}{\rho}\mathrm{d}p = -q\mathrm{d}q \tag{16}$$

where γ denotes specific heat ratio of gas.

The aerodynamic parameter of each point in the flowfield can be obtained by solving the above equations with numerical programme, which mainly includes two types of points: field point and body point. The reference plane method is adopted, and the entry plane of the flowfield is taken as the initial reference plane, which is discretised into a series of parameter points for a given aerodynamic condition. The process is calculated from the known reference plane to the new reference plane along the flow direction and repeated until the last reference plane is calculated. The distance dz of different reference planes must satisfy Courant-Friedrichs-Lewy (CFL) stability conditions, and the specific solution method of element points along the Mach conoid can be referred to Ref. (30).

2.2 Theory of maximum thrust nozzle

As shown in Fig. 2, the theory of maximum thrust nozzle design [12] refers to the design of the maximum thrust nozzle under certain nozzle length and mass flow constraints by using the Lagrange multiplier method, which has obvious advantages and is widely used in nozzle design.

Under the constraints of Equations (17–19), the maximum value of the system of equation is obtained by the Lagrange multiplier method.

$$\dot{m}_{EC} = \int_E^C \rho v\frac{\sin(\varphi-\theta)}{\sin\varphi}2\pi y\mathrm{d}y = const \tag{17}$$

$$L_n = x_E + \int_E^C \cot\varphi\mathrm{d}y \tag{18}$$

$$F = \int_E^C \left[(p-p_0) + \rho v^2\frac{\sin(\varphi-\theta)\cos\theta}{\sin\varphi}\right]2\pi y\mathrm{d}y \tag{19}$$

https://doi.org/10.1017/aer.2026.10153 Published online by Cambridge University Press

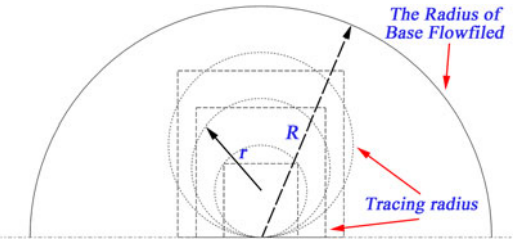


Figure 3. *Schematic diagram of different tracing profile and radius at the entrance of the parent flowfield.*

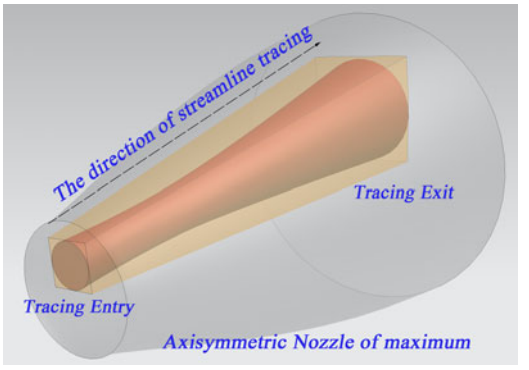


Figure 4. *The direction of streaming tracing in the parent flowfield.*

Here, an equation along the EC line of the control plane needs to be added:

$$\varphi = \theta + \alpha \tag{20}$$

Because point C is on the left-hand characteristic line from point E, the following relationship also exists:

$$\sin(2\theta_C) = \frac{(p_c - p_0)\cot(\varphi - \theta)}{\frac{1}{2}v_C^2\rho_C} \tag{21}$$

The streamline angle θ and Mach angle α on the EC line of the control surface also have the following relationship:

$$\frac{v\cos(\theta - \alpha)}{\cos\alpha} = C_1 \tag{22}$$

$$y\rho v^2 \sin^2\theta \tan\alpha = C_2 \tag{23}$$

2.3 Nozzle design method

In this paper, the parent flowfield is constructed based on 3D MOC, and the nozzle profile is designed by streamline tracing method. As shown in Figs 3 and 4, the aerodynamic configuration of 3D nozzle can be obtained by taking the entry semicircular area of the parent flowfield as the initial surface and tracing a predetermined entry profile from inlet to outlet in the parent flowfield. It can be seen from Section 2.1 that 3D MOC solves the swirling flow equation, and the corresponding points on the upstream and downstream of reference planes in the flowfield are solved along the streamlines and Mach conoid. It is also a remarkable feature of 3D MOC that the connecting lines of corresponding points on the reference planes in the flowfield are streamlines. Then the nozzle profile formed by tracing based on the parent flowfield is an asymmetric nozzle with the outlet cross section perpendicular to the axis. It is worth noting that the flowfield downstream of the last left-running characteristic (along CE in Fig. 2)

https://doi.org/10.1017/aer.2026.10153 Published online by Cambridge University Press

has no influence on the nozzle profile and turning region, so the profile shearing method [27] is used to obtain the inviscid SERN. Finally, the complete 3D nozzle geometry is then reconstructed through surface fitting in Computer-Aided Design (CAD), ensuring geometric continuity and smooth curvature between all wall boundaries.

2.4 Boundary layer correction

In order to fully consider the influence of boundary layer on the flowfield of SERN, the reference temperature method [13] is used to modify the boundary layer.

The displacement thickness of boundary layer δ_1 can be determined as follows:

$$\frac{\delta_1}{x}\sqrt{Re_x} = \sqrt{N^*}\left[5.0 + \left(0.2 + \frac{0.9T_w}{T_{aw}}\right)(\gamma - 1)\,Ma_{pri}^2\right] \tag{24}$$

where Re_x is the local Reynolds number, Ma_{pri} represent the Mach number of the primary flow in the nozzle and T_w and T_{aw} are wall temperature and adiabatic wall temperature of the nozzle, respectively. This study assumes $T_w/T_{aw} = 1$.

The variable N^* can be determined as follows:

$$N^* = \left(\frac{T^*}{T_{pri}}\right)^{n-1} \tag{25}$$

where T^* is the reference temperature, which can be determined as follows:

$$\frac{T^*}{T_{pri}} = 0.5 + 0.5\frac{T_w}{T_{pri}} + 0.0283Ma_{pri}^2 \tag{26}$$

where T_{pri} is the mainstream temperature of the airflow, and n is 0.81 in this paper.

T_w can be calculated as follows:

$$\frac{T_t - T_w}{T_0 - T_w} = \frac{u_b}{u_e} \tag{27}$$

where T_t, T_0, u_b, u_e are the total temperature in the nozzle, ambient temperature, airflow velocity in the boundary layer and airflow velocity between the boundary layer and the mainstream, respectively.

The boundary layer thickness is added to the traced streamline by the transforming coordinate, so as to obtain final the nozzle configuration, which can meet the viscous need of actual gas flow in the nozzle. The profile comparison of the top wall and circumferential wall before and after boundary layer correction are shown in Fig. 5, where *Z/r* and *R/r* represent the ratio of wall axial distance and wall radial distance to entry radius of SERN. According to the reference temperature method, the boundary layer thickness is affected by temperature, Mach number and axial distance, so the circumferential wall generated by streamline tracing is closer to the centre in the three-dimensional parent flowfield. As Fig. 5 shows, the boundary layer on the circumferential wall is thicker than that on the top wall in the same axial position and the maximum thickening of the wall along the radial direction reaches 0.89% at $Z/r = 8$, which show the change of the flow parameter along the radial direction in the whole parent flowfield.

3.0 Numerical simulation method

3.1 Numerical method

To obtain the detailed flowfield and performance of the designed SERN, the three-dimensional, steady and compressible Reynolds-averaged Navier-Stokes (RANS) equations coupled with the shear-stress transport (SST) k-ω turbulence model are solved numerically, which provides a good balance between accuracy and computational efficiency for external aerodynamic flows involving both boundary layer separation and adverse pressure gradients. The governing equations, which include the conservation

https://doi.org/10.1017/aer.2026.10153 Published online by Cambridge University Press

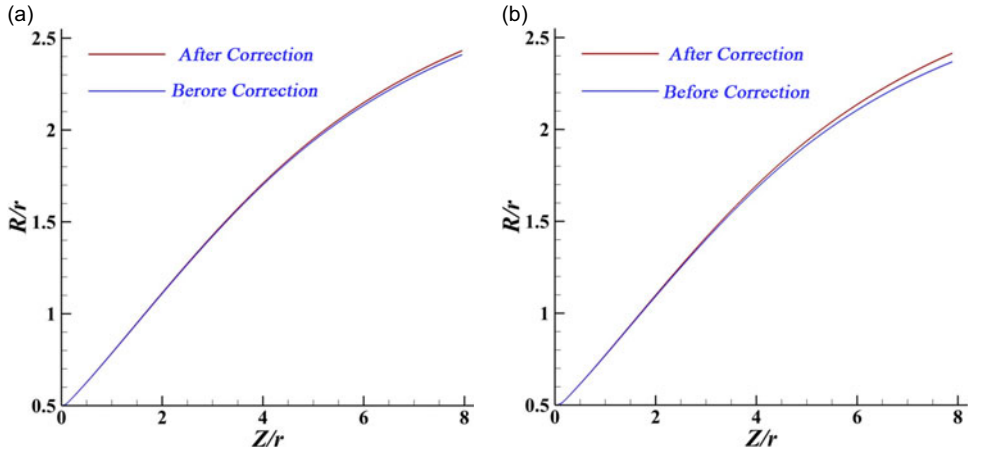


Figure 5. *Comparison of SERN wall profile before and after boundary layer correction.*

equations for mass, momentum and energy, are shown as follows:

$$\frac{\partial Q}{\partial t}+\frac{\partial E}{\partial x}+\frac{\partial F}{\partial y}+\frac{\partial G}{\partial z}=0 \tag{28}$$

where

$$Q=\begin{bmatrix}\rho\\ \rho u\\ \rho v\\ \rho w\\ \rho e\end{bmatrix} \qquad E=\begin{bmatrix}\rho u\\ \rho u^2+p-\tau_{xx}\\ \rho uv-\tau_{xy}\\ \rho uw-\tau_{xz}\\ u(\rho e+P)-u\tau_{xx}-v\tau_{xy}-w\tau_{xz}\end{bmatrix}$$

$$F=\begin{bmatrix}\rho v\\ \rho vu-\tau_{yx}\\ \rho v^2+p-\tau_{yy}\\ \rho vw-\tau_{yz}\\ v\,(\rho e+P)-u\tau_{yx}-v\tau_{yy}-w\tau_{yz}\end{bmatrix} \qquad G=\begin{bmatrix}\rho w\\ \rho wu-\tau_{zx}\\ \rho wv-\tau_{zy}\\ \rho w^2+p-\tau_{zz}\\ w(\rho e+P)-u\tau_{zx}-v\tau_{zy}-w\tau_{zz}\end{bmatrix}$$

and

$$\begin{aligned}\tau_{xx} &= -\tfrac{2}{3}\mu(\nabla\cdot\bar{V})+2\mu\tfrac{\partial u}{\partial x}, & \tau_{yy} &= -\frac{2}{3}\mu(\nabla\cdot\bar{V})+2\mu\frac{\partial v}{\partial y},\\ \tau_{zz} &= -\tfrac{2}{3}\mu(\nabla\cdot\bar{V})+2\mu\tfrac{\partial w}{\partial z}, & \tau_{xy} &= \tau_{yx}=\mu\left(\frac{\partial u}{\partial x}+\frac{\partial v}{\partial y}\right),\\ \tau_{yz} &= \tau_{zy}=\mu\left(\tfrac{\partial v}{\partial y}+\tfrac{\partial w}{\partial z}\right), & \tau_{xz} &= \tau_{zx}=\mu\left(\frac{\partial u}{\partial x}+\frac{\partial w}{\partial z}\right)\\ e &= 0.5(u^2+v^2+w^2)+\tfrac{p}{\rho}\end{aligned}$$

The viscosity μ is given by the following:

$$\mu=\mu_l+\mu_t \tag{29}$$

The laminar viscosity μ_l is calculated by Sutherland's law, as shown in Equation (30):

$$\mu_l=\mu_{ref}\left(\frac{T}{T_{ref}}\right)^{3/2}\frac{T_{ref}+T_s}{T+T_s} \tag{30}$$

https://doi.org/10.1017/aer.2026.10153 Published online by Cambridge University Press

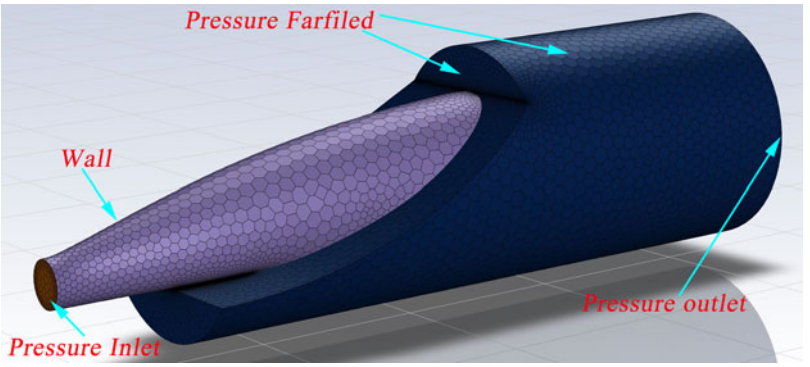


Figure 6. *Computational domain and mesh distribution of nozzle.*

where μ_{ref}, T_{ref} and T_{s} are the reference viscosity, reference temperature and effective temperature, respectively, which correspond to $1.76 \times 10 - 5$Pa•s, 273.11k and 110.56k.

The turbulent viscosity μ_{t} is obtained from the SST k-ω two-equation model, and the turbulence kinetic energy k and its specific dissipation rate of turbulence ω are obtained from the following transport equations:

$$\frac{\partial(\rho k)}{\partial t} + \frac{\partial(\rho u_i k)}{\partial x_i} = \frac{\partial}{\partial x_i}\left[(\mu_l + \sigma_k \mu_t)\frac{\partial k}{\partial x_i}\right] + P_k - \beta^* \rho \omega k \tag{31}$$

$$\frac{\partial(\rho \omega)}{\partial t} + \frac{\partial(\rho u_i \omega)}{\partial x_i} = \frac{\partial}{\partial x_i}\left[(\mu_l + \sigma_\omega \mu_t)\frac{\partial \omega}{\partial x_i}\right] + P_\omega - \beta \rho \omega^2 + 2(1 - F_1)\frac{\rho \sigma_{\omega^2}}{\omega}\frac{\partial k}{\partial x_i}\frac{\partial \omega}{\partial x_i} \tag{32}$$

where ρ is the density, p is the pressure, u_{i} is the i_{th} component velocity, τ_{ij} is the shear stress term, P_{k} and P_{ω} denote production terms of the turbulent kinetic energy k and the specific dissipation rate of turbulence ω, respectively, μ_{l} and μ_{t} are the laminar and turbulent viscosity, F_1 is auxiliary functions, σ_{k}, σ_{ω}, β and β^* are model constants.

The governing equations are discretised by the finite-volume method, and the second-order upwind scheme is used to discretise the viscous flux. Also, standard wall functions are introduced to model the near-wall region flow, and a non-slip, adiabatic condition is imposed on the wall. The CFL number is set as 0.5 to ensure the numerical stability. The solution was considered converged when the normalised residuals of all governing equations fell below 1×10^{-4}, and the thrust coefficient variation between iterations was less than 0.1%.

The boundary conditions were defined as shown in Fig. 6. The inlet of the far-field and surrounding boundaries was set as pressure far-field conditions to represent the freestream environment, while outlet of the far-field was specified as a pressure-outlet condition to ensure smooth flow expansion. The nozzle inlet was imposed as a pressure-inlet condition corresponding to the designed total pressure and temperature. For the post-processing, the steady-state flowfield data were extracted after achieving convergence, and flow variables such as static pressure, Mach number and density were visualised on the symmetry plane and selected cross-sections.

3.2 Numerical method validation

Wdtanahc [31] of NAL in Japan has conducted many experiments on SERN in a hypersonic wind tunnel. The obtained experimental data under the condition of different Mach numbers and pressure ratios has been unanimously recognised by relevant researchers. As Fig. 7 shows, the experimental nozzle is numerically simulated, whose boundary conditions are listed in paper [31]. Under the incoming flow condition of Mach number 7.1 in wind tunnel, two nozzle test models with inlet total pressure of 145 kPa and 39 kPa were selected, which were denoted as Case 1 and Case 2.

https://doi.org/10.1017/aer.2026.10153 Published online by Cambridge University Press

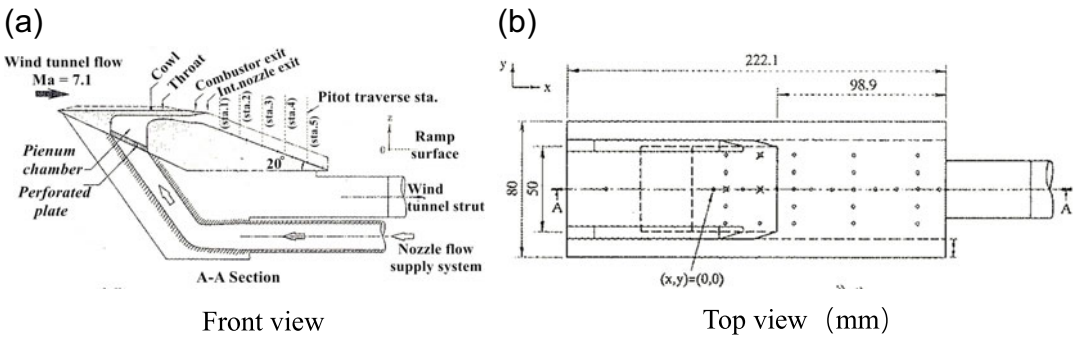


Figure 7. *Geometry schematic of test model in NAL [31].*

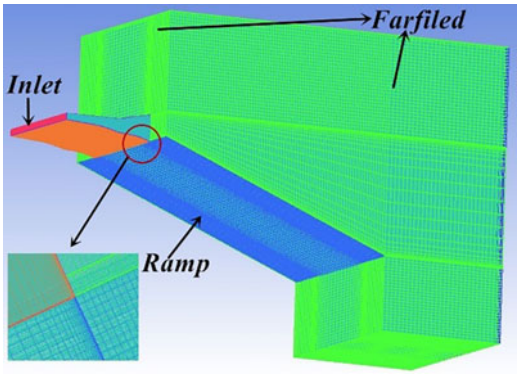


Figure 8. *Computational domain and mesh distribution of nozzle.*

Figure 8 presents the computational mesh of the SERN under the experimental operating condition. The total grid number is approximately 0.9 million. The boundary conditions at the nozzle inlet, outlet and extended surfaces are specified as pressure inlet, pressure outlet and pressure farfield, respectively. To ensure computational accuracy, local mesh refinement was applied in key flow regions, including the nozzle throat, near-wall zones and shear layers, to accurately capture the flow gradients and shock–boundary-layer interactions. The mesh distribution demonstrates a balanced resolution between computational efficiency and numerical precision, providing a reliable basis for the subsequent validation and performance analysis.

As Fig. 9 shows, it can be seen that the numerical calculation result captures the flow characteristics of nozzle exit well, which is in good agreement with the shadow-graph measured from the experiment. Figure 10 further shows the pressure distribution of a down wall obtained by Case 2, from which we can see that the numerical result is consistent with the experimental data and can accurately reflect the change trend of pressure. Therefore, it is considered that the adopted numerical method can be used to simulate three-dimensional nozzle flowfield.

3.3 Mesh independence verification

The grid independence study is conducted to determine the appropriate grid resolution, so different bottom mesh thicknesses ($h = 0.02$ mm, $h = 0.04$ mm, $h = 0.06$ mm, $h = 0.09$ mm, $h = 0.12$ mm) are selected to carry out the independence analysis of bottom mesh size. The performance parameters (treated by mass-weighted average, $Ma = 6.0$) on the nozzle exit by changing with the thickness of the bottom grid are listed in Table 1. It can be seen that the thrust coefficient and exit Mach number change

https://doi.org/10.1017/aer.2026.10153 Published online by Cambridge University Press

Table 1. *Performances at the outlet of nozzle vary with minimum spacing*

h/mm	Thrust coefficient	Ma_{out}	y+
0.02	0.969	3.741	1.14
0.04	0.969	3.740	1.92
0.06	0.964	3.737	2.88
0.09	0.958	3.730	5.32
0.12	0.947	3.718	7.76

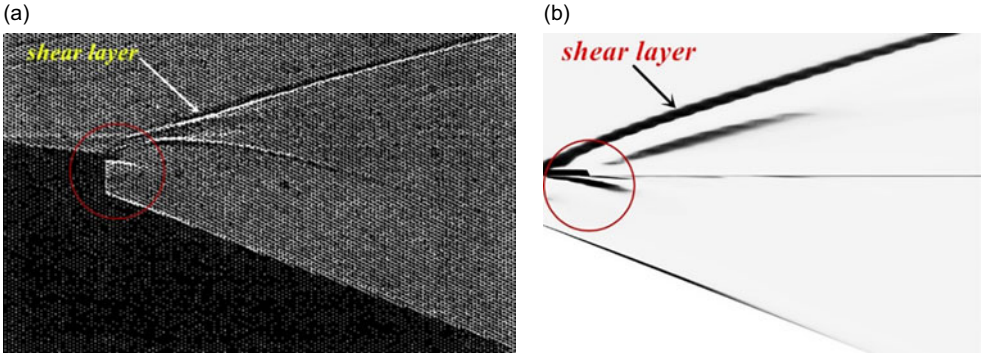


Figure 9. *Comparison of shadow-graph photo between experiment and calculation (Case1).*

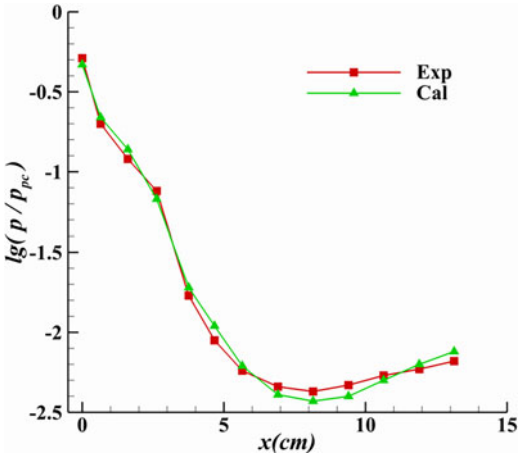


Figure 10. *Surface pressure along the ramp of NAL SERN obtained from the experiment and numerical simulation (Case 2).*

greatly when $h > 0.06$ mm. Comparing with $h = 0.02$ mm and $h = 0.04$ mm, the thrust coefficient and exit Mach number are almost unchanged, which obviously meets the requirements of grid independence. Therefore, the bottom mesh size selected as calculation is performed on the grid of 0.04 mm ($y^+ \asymp 1.9$).

In order to reduce the influence of mesh size on calculation results, three structured computational grids with different grid resolution, namely coarse (6,80,000 cells), medium (9,80,000 cells) and fine (1.34 million cells) grids, are generated for the nozzle designed by the proposed method. Figure 11 illustrates the mesh distributions at different grid densities, highlighting the refinement near the nozzle outlet, wall surfaces and shear layer regions used for the mesh independence verification. Under the inflow condition of $Ma = 6.0$, the pressure distribution on the down wall of different scale grids is shown

https://doi.org/10.1017/aer.2026.10153 Published online by Cambridge University Press

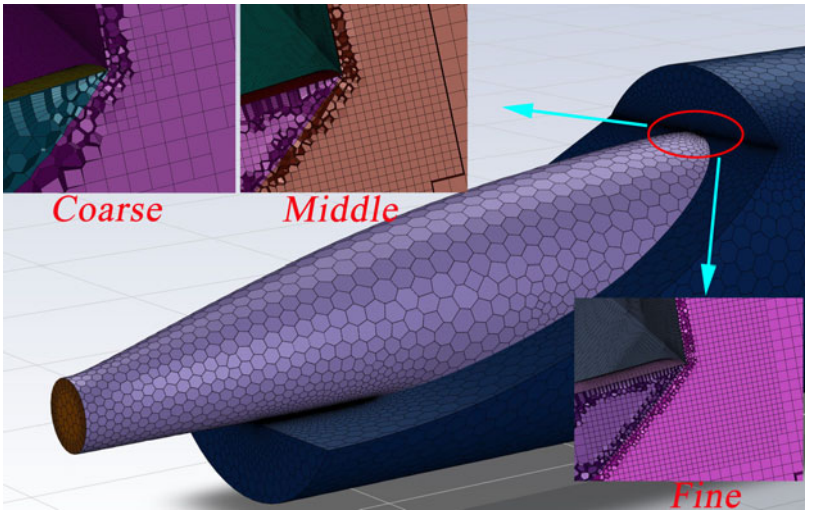


Figure 11. *Mesh distributions at different grid densities for the mesh independence.*

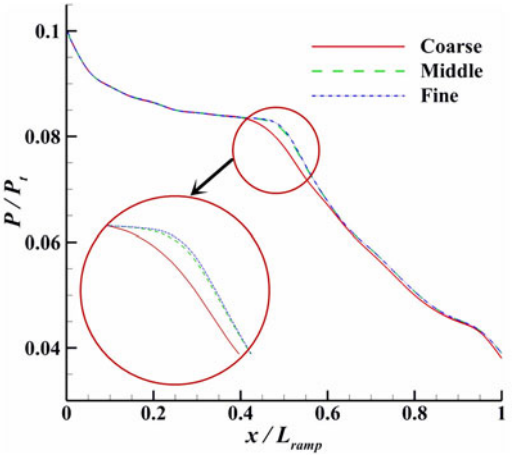


Figure 12. *Pressure distribution on the ramp obtained from the different scale grids.*

in Fig. 12, from which it can be seen that the pressure distribution in a coarse grid has a large deviation compared with the other two-scale grids near $x/L_{\text{ramp}} \approx 0.46$, while the pressure distribution of medium and fine is consistent. It is concluded that the numerical results are almost unaffected by the increase of mesh numbers when reaching 980,000. These results show that the medium grid resolution can be used to obtain an accurate result, which is adopted in the subsequent numerical simulations.

3.4 Definitions of nozzle performance parameters

Parameters such as axial thrust coefficient C_{fx}, lift coefficient C_y and pitching moment M are important to quantify the nozzle performance. The axial thrust coefficient reflects the propulsion efficiency of the nozzle, while the lift and pitching moment play a vital role in balancing the head-up moment produced by the forebody and inlet.

The axial thrust F_{cx} is calculated as:

$$F_{cx} = \dot{m} v_{inx} + (p_{inx} - p_0) A_{\text{inx}} - R_x \tag{33}$$

https://doi.org/10.1017/aer.2026.10153 Published online by Cambridge University Press

Table 2. *Airflow condition of design point*

Ma_c	*H/km*	Ma_{in}	*Tt/K*	p_t */kPa*
6.0	26.0	1.68	2430	389

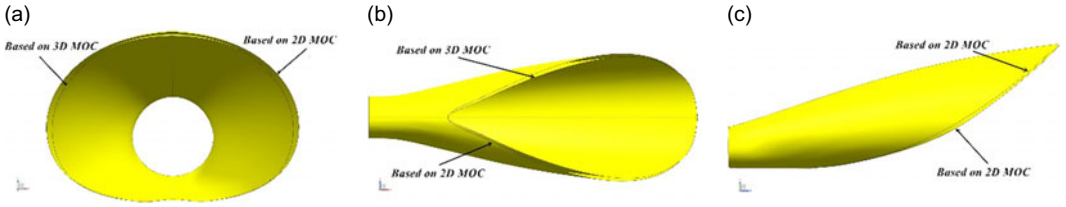


Figure 13. *Profile comparison of 3D SERN with specific heat based on 2D MOC and 3D MOC.*

where v_{inx}, p_{inx}, A_{inx}, p_0, R_x are the nozzle entry axial velocity, static pressure, axial projection area of entry, ambient pressure and axial thrust, respectively.

The isentropic thrust of the nozzle is denoted as F_s, which can be calculated as follows:

$$F_s = \dot{m}\sqrt{\frac{2\gamma}{\gamma-1}RT_t\left(1-\left(\frac{1}{\pi}\right)^{\frac{\gamma-1}{\gamma}}\right)} \tag{34}$$

$$\pi = p_t/p_0 \tag{35}$$

where R, T_t, p_t are the gas constant, total temperature, and total pressure, respectively. π is defined as pressure drop ratio of the nozzle.

Finally, C_{fx} and C_y are calculated as follows:

$$C_{fx} = \frac{F_{cx}}{F_s} \tag{36}$$

$$C_y = \frac{F_y}{q_0 A} \tag{37}$$

where q_0 and F_y, A are the dynamic pressure of free stream, lift, and maximum projected area along the axial direction.

The reference point of M is the centre of the nozzle entry.

4.0 Result and discussion

4.1 Comparative analysis of the nozzle characteristics based on 2D MOC and 3D MOC

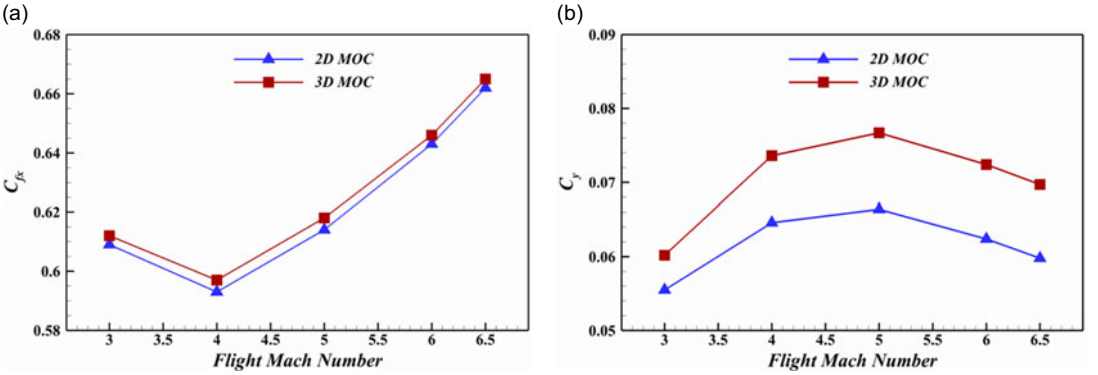
In order to prove the superiority of the nozzle design method based on 3D MOC, the characteristics of the nozzle designed by 3D MOC are compared with those designed by traditional 2D MOC design. According to the design conditions shown in Table 2 and the constraint of the same length, the 3D SERN profile with specific heat is obtained based on 2D MOC and 3D MOC. As shown in Fig. 13, the exit cross-sectional profiles of the two nozzles exhibit slight differences from the front view, indicating that the axial projected area of the nozzle designed using the 3D MOC method is approximately 1.4% smaller than that of the nozzle obtained from the 2D MOC method. This result suggests a slightly more compact expansion contour in the three-dimensional design. Moreover, from the vertical and side view. the profile difference of two nozzles is mainly manifested in the circumferential wall, which is the superposition effect of streamline tracing in different parent flowfields and using reference temperature method.

In addition to the airflow conditions listed in Table 2, two nozzles designed by 2D MOC and 3D MOC are numerically simulated under other typical flight conditions listed in Table 3. Figure 14 shows

https://doi.org/10.1017/aer.2026.10153 Published online by Cambridge University Press

Table 3. *Airflow conditions of typical flight Mach number*

Ma_c	*H/km*	Ma_{in}	T_t/*K*	p_t/*kPa*
6.5	27.0	1.80	2500	480
5.0	23.6	1.48	2160	316
4.0	20.7	1.25	2030	240
3.0	16.0	1.05	1970	195



Axial thrust coefficient Lift coefficient

Figure 14. *Variation of axial thrust coefficient and lift coefficient with flight Mach number.*

the performance comparison of the two nozzles under different flight Mach number, from which it can be seen that the performance of the two nozzles has the same change trend with the improvement of flight Mach number. The axial thrust coefficient decreases at first and then increases, which is minimum when $Ma = 4.0$ and reaches maximum when $Ma = 6.5$. Moreover, the lift coefficient first increased and then decreased, which reaches the maximum when $Ma = 5.0$. Compared with the nozzle designed by 2D MOC, the axial thrust coefficient of the nozzle designed by 3D MOC is increased by more than 0.45%. With the increase of the Mach number, the increment of the axial thrust coefficient first increases and then decreases, whose maximum increases are 0.675% at $Ma = 4.0$ and 0.467% at $Ma = 6.0$. The lift coefficient showed a substantial increase with increasing Mach number, except at $Ma = 3.0$, with increases of more than 13% observed in all other cases. Besides that, the lift coefficient increases with the increase of the flight Mach number, reaching the maximum value of 16.6% at $Ma = 6.5$ and increasing by 16.0% at $Ma = 6.0$.

Figure 15 shows the pressure contours of two nozzles based on 2D MOC and 3D MOC in the central section under a typical flight Mach number, in which the distance between the two red auxiliary dotted lines clearly marks the axial distance of the weak expansion wave on the upper wall of the two nozzles. It can be observed that the position of expansion waves from the entry of the upper wall to the exit of the lower wall move upstream in the flowfield with the decrease of the flight Mach number. Compared with the nozzle designed by 3D MOC, the position of expansive waves of the nozzle designed by 2D MOC is closer to the upstream in the flowfield, and the weak expansive wave is especially obvious. With the increase of the flight Mach number, the position interval of expansion waves on the upper wall of the two nozzles gradually increases and the shocks downstream of the nozzle exit is closer to the upstream in the flowfield at $Ma = 3.0$. Thus, the position change of the expansion waves and the shocks downstream of the nozzle has a significant influence on the flowfield. The position change of expansion waves along the axial direction will lead to the difference of the pressure at the same position of the nozzle, which will directly affect the effort of the airflow on the upper wall. This also explains why the nozzle designed by 3D MOC has better performance, and the increase of lift coefficient is particularly obvious.

https://doi.org/10.1017/aer.2026.10153 Published online by Cambridge University Press

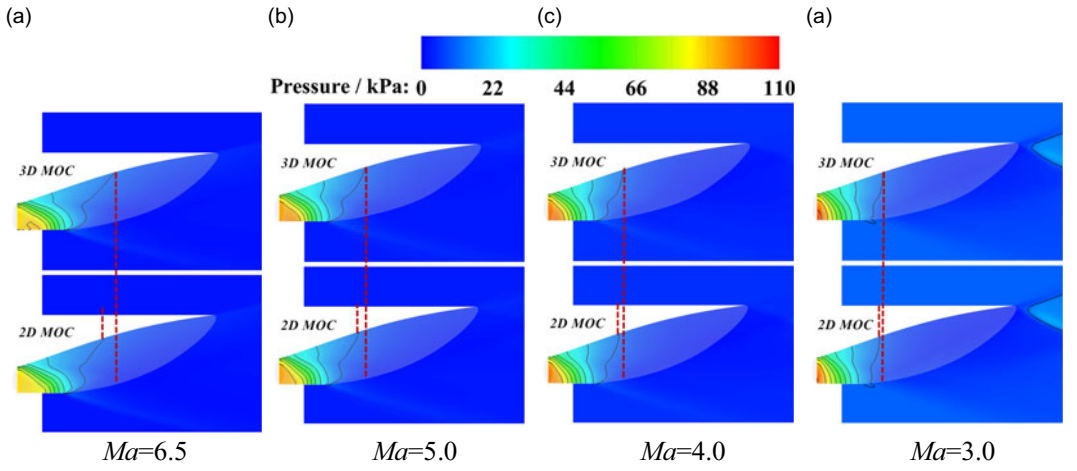


Figure 15. *Comparison of pressure distribution on the cross section between two nozzles.*

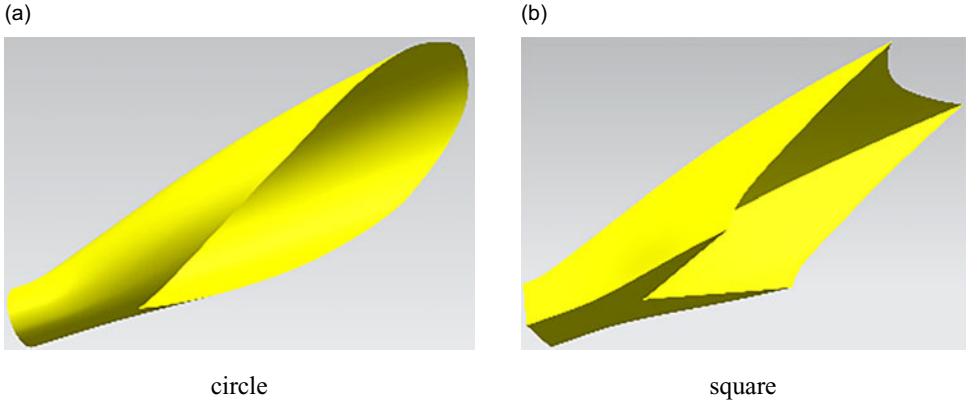


Figure 16. *Aerodynamic configurations obtained from different entry profiles.*

4.2 Influence of tracing profile on nozzle performance

Based on 3D MOC, the flowfield and performance of nozzle tracing by different profiles are further discussed. As Fig. 16 shows, the circular nozzle and the rectangular nozzle are great differences, which are obtained by the same area of the tracing profile under the design conditions in Table 2. It is noted that the upper wall of the rectangular nozzle forms an arc-curved surface, which appears short on the middle and long on the side, while the lower wall forms a unique sharp angle. For the convenience of the following description, the rectangular nozzle is denoted as Nozzle A and the circular nozzle is denoted as Nozzle B.

Table 4 shows performance comparison involved the axial thrust coefficient, lift coefficient and pitching moment of the two nozzles. It can be seen that compared with the difference of profiles, there is little difference in performance between two nozzles. The axial thrust coefficient and lift coefficient of Nozzle B are slightly improved compared to Nozzle A, while the pitching moment is improved with the increase reaching 9.6%. Figure 17 shows the pressure contours in the central section and isosurfaces of two nozzles, in which the red vertical auxiliary line is used to compare the position of the leading edge on the pressure isosurface near the upper wall. It can be seen that the pressure distribution of the two nozzles is similar, while there is a slight difference in the position of the pressure isosurface. Moreover, comparing with Nozzle A, the expansion of Nozzle B is slightly slower in the initial stage and faster in the

https://doi.org/10.1017/aer.2026.10153 Published online by Cambridge University Press

Table 4. *Performance comparison between Nozzle A and Nozzle B*

	C_{fx}, N	C_L, N	M, N•m
Nozzle A	0.647	0.0247	321.91
Nozzle B	0.649	0.0249	352.94
Δ	0.3%	0.8%	9.6%

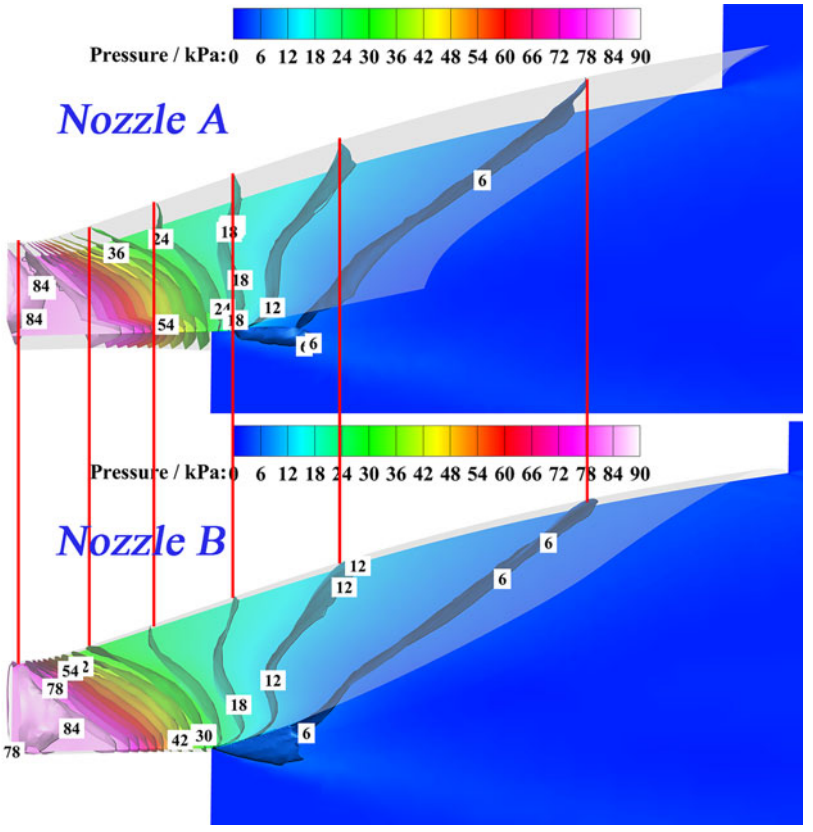


Figure 17. *Comparative contour and isosurface of pressure in the central section of Nozzle A and Nozzle B.*

downstream, which can be seen from the pressure isosurface from 36kPa to 6kPa. In addition, due to the difference of exit profiles, the shape of isosurface changes from almost the same to slightly different along the flow direction, especially there are obvious differences between Nozzle A and Nozzle B near the sharp corner on the exit of the lower wall. This is the reason why the lift and pitching moment of Nozzle B is higher than that of Nozzle A.

Compared with the profile of a conventional 2D rectangular nozzle, Nozzle A has some differences in upper and lower walls. In order to explore the differences in flowfield and performance between Nozzle A and the conventional 2D rectangular nozzle, three new nozzles are obtained by filling up the circular arc surface of the upper wall and the sharp corner of the lower wall on the basis of Nozzle A. As Fig. 18 shows, new nozzles are named Nozzle A-1, Nozzle A-2 and Nozzle A-3 in turns for convenience of description, among which Nozzle A-3 is similar to the profile of 2D rectangular nozzle with lateral expansion. The annotated 'Fill-up' regions indicate the modified wall surfaces relative to

https://doi.org/10.1017/aer.2026.10153 Published online by Cambridge University Press

Table 5. *Performance comparison between Nozzle A and three new nozzles*

	C_{fx}, N	C_L, N	M, N•m
Nozzle A	0.647	0.0247	321.91
Nozzle A-1	0.646	0.0283	350.30
Nozzle A-2	0.648	0.0044	269.86
Nozzle A-3	0.647	0.0091	300.39
Δ(A-1/A)	−0.15%	14.6%	8.8%
Δ(A-2/A)	0.15%	−82.2%	−16.2%
Δ(A-3/A)	0	−63.2%	−6.7%

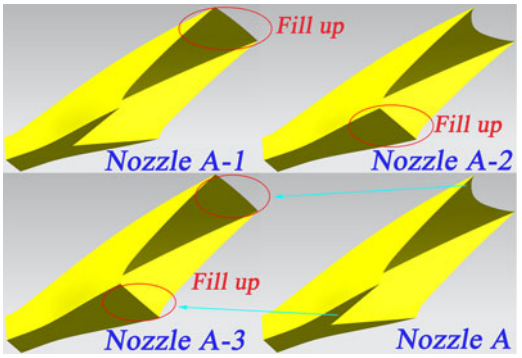


Figure 18. *The profiles of new nozzles based on Nozzle A.*

the baseline Nozzle A. The variations correspond to different filling positions on the upper and lower walls, illustrating how local geometric adjustments were applied to study their influence on the overall aerodynamic performance.

Comparing the performance of nozzles listed in Table 5, it can be seen that the change of upper and lower walls has relatively little influence on axial thrust. It is worth noting here that the axial thrust coefficient decreases and increases by 0.15%, respectively, after filling up the profile of upper and lower walls, while the axial thrust coefficient remains unchanged after filling up both (Nozzle A-3). Moreover, the influence of profile on lift and pitching moment is obvious that lift coefficient and pitching moment increase by 14.6% and 8.8%, respectively, when the profile of the upper wall is filled, decrease by 82.2% and 16.2%, respectively, when the profile of the lower wall is filled. So it can be seen that the profile to be filled has a great influence on the lift and pitching moment. Besides that, the lift coefficient and pitching moment of Nozzle A-3 are reduced by 63.2% and 6.7%, respectively, which shows that the sharp angle surface filled in the lower wall has greater influence on the lift and pitching moment.

As Fig, 19 shows, when comparing Nozzle A with Nozzle A-1, it can be seen that the flowfield has little change after filling up the upper wall, which appears that the isosurface moves forward slightly on the upper wall, and the isosurface at the sharp corner of the lower wall moves upward and integrates with the isosurface of 6kPa. Comparing Nozzle A with Nozzle A-2, as displayed in Fig. 19, the lower wall to be filled directly affects the shape of the isosurface, whose position on the upper wall moves downstream and the range of movement increases continuously. The change of the surface and position can be clearly seen on the isosurface of 6kPa. Compared with Nozzle A-2 and Nozzle A-3, it can be seen that the flowfield changes little and the shape of isosurface changes slightly whose position on the upper wall moves slightly upstream approaching the isosurface of Nozzle A. Therefore, it is obtained that the change of the profile causes the intuitive change of the isosurface. The upper and lower walls to

https://doi.org/10.1017/aer.2026.10153 Published online by Cambridge University Press

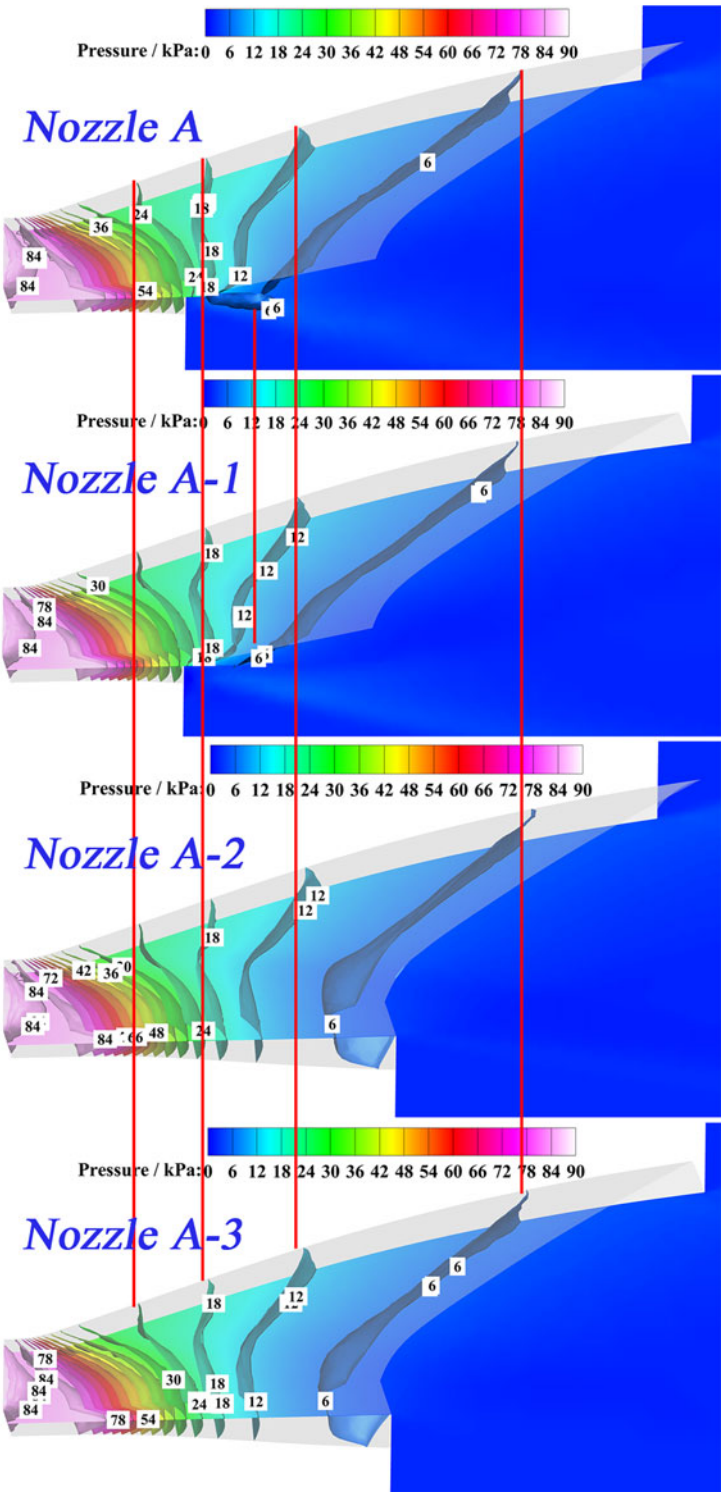
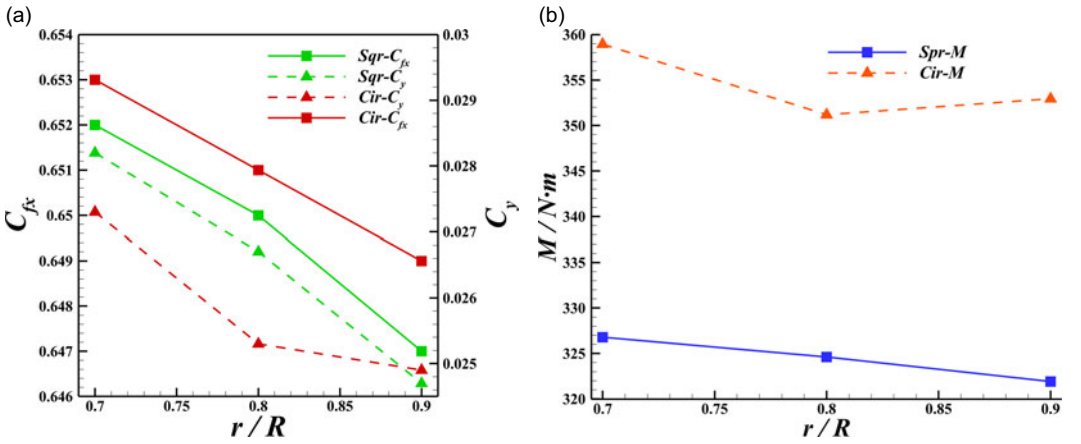


Figure 19. *Comparative contour of pressure distribution in the central section of Nozzle A and three new nozzles.*

https://doi.org/10.1017/aer.2026.10153 Published online by Cambridge University Press



axial thrust coefficient and lift coefficient

pitching moment

Figure 20. *Variances of the nozzle performances with the increase of the tracing radius.*

be filled mainly affects the position and shape of isosurface, which is finally reflected in the change of nozzle performance.

From the above results discussed, it can be seen that the axial thrust of the nozzle has little change after filling the profile, while the lift and pitching moment have great change, which can increase the selectivity for the nozzle design. According to the geometric limitations, lift requirements and moment matching requirements, the design of aerodynamic nozzle profile can be carried out flexibly.

4.3 Influence of tracing radius on nozzle performance

Based on Nozzle A and Nozzle B discussed in Section 4.2, the effects of the different tracing radius ($r/R = 0.7, 0.8, 0.9$) on the flowfield and performance of the nozzle ensuring the same entry area are further discussed according to the design conditions listed in Table 2. For the convenience of the following description, the newly generated nozzles are denoted as Nozzle A-r0.8, Nozzle A-r0.7, Nozzle B-r0.8 and Nozzle B-r0.8, respectively, according to the different tracing radius.

As shown in Fig. 20(a), the tracing radius can significantly affect the axial thrust coefficient and lift coefficient of Nozzle A and Nozzle B, which decrease with the increase of tracing radius. Compared with the case of $r/R = 0.7$, when $r/R = 0.9$, the axial thrust coefficients of the Nozzle A and Nozzle B are reduced by 0.8% and 0.6%, respectively, while the lift coefficients are reduced by 12.4% and 8.8%, respectively. It indicates that the change of the tracing radius has a dominant impact on the lift coefficient, and Nozzle A is more likely to be affected. Unlike the obvious decrease of the lift coefficient, as displayed in Fig. 20(b), the increase of the tracing radius only has a slight influence on the nose-down pitching moment. In addition, the nose-down pitching moment of Nozzle B slightly decreases and then increases with the change of the tracing radius, which also corresponds to the turning point of the lift coefficient when $r/R = 0.8$ shown in Fig. 20(a).

The pressure contours of Nozzle A and Nozzle B with different tracing radii are displayed in Fig. 21(a), in which the red vertical auxiliary line has the same effect as mentioned in Section 4.2. By comparing Nozzle A, Nozzle A-r0.8 and Nozzle A-r0.7, it can be seen that the flowfield of the initial expansion section and the area of the lower wall has little change under different tracing radii, whose differences are mainly reflected in the position change of the isosurface on the upper wall. Furthermore, with the increase of the tracing radius, the isosurfaces at the upper wall from 6kPa to 24kPa move upstream and the amplitude increases continuously, and the shape of isosurfaces gradually widens after deflection to the side at the same time. Figure 21(b) shows the pressure comparison of flowfields among

https://doi.org/10.1017/aer.2026.10153 Published online by Cambridge University Press

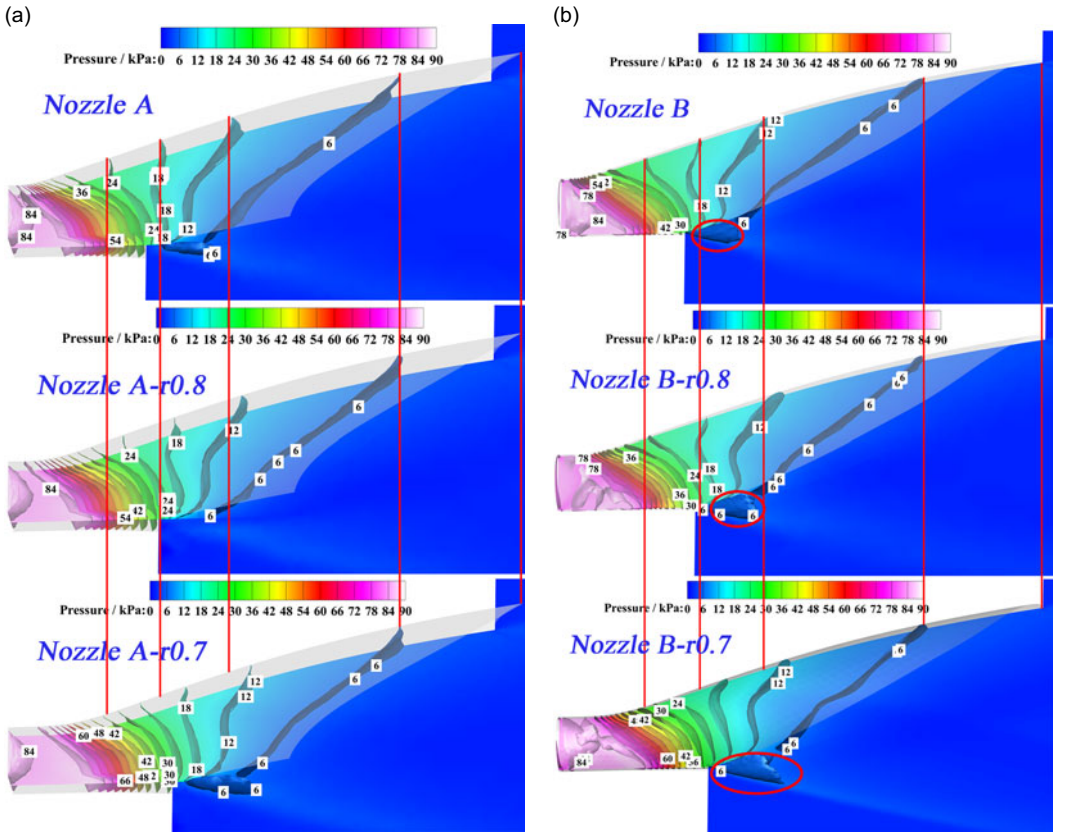


Figure 21. *Comparative contour of pressure distribution in the central section of Nozzle A and Nozzle B with different tracing radii.*

Nozzle B, Nozzle B-r0.8 and Nozzle B-r0.7, in which the position of the isosurface on the upper wall has the same trend as that shown in Figure 21(a) with the increase of tracing radius, while the movement amplitude decreases slightly. Compared with Figure 21(a), the isosurfaces in the initial expansion section and over the lower-wall region show significant differences, particularly in the exit region highlighted by the red ellipse on the lower wall, where the isosurface shape changes noticeably.

Therefore, it can be seen that the various radii leads to differences in the position and shape of the isosurface as well as the flowfield of the outlet. The position change of the isosurface on the upper wall has a slight influence on the axial thrust coefficient, but has a greater influence on the lift coefficient, which is consistent with the conclusion obtained from the analysis of the flowfield in Section 4.2. It is worth noting that as the tracing radius increases, the characteristic that the lift changes more while the nose-down pitching moment changes little adds flexibility to the nozzle design when considering the requirements of the lift and matching moment both.

5.0 Conclusion

This study proposes a three-dimensional nozzle design approach based on the 3D MOC to enhance aerodynamic performance. The proposed 3D MOC design method allows the nozzle to better preserve the true three-dimensional characteristics of the parent flowfield compared with the conventional 2D MOC approach. The flow structures and aerodynamic performances of nozzles designed by both methods were

https://doi.org/10.1017/aer.2026.10153 Published online by Cambridge University Press

compared and analysed, followed by an investigation of different entry-tracing profiles and geometric radii.

The following conclusions are drawn:

(1) The main profile difference between the nozzles designed by 2D MOC and 3D MOC occurs along the circumferential wall. Under typical flight conditions, the expansion wave and shock structures in the 3D MOC–designed nozzle are shifted further downstream, leading to an increase of over 0.45% in axial thrust coefficient and more than 8% in lift coefficient.

(2) The comparison between the RN and CN shows that, while their overall flowfields are similar, the CN provides higher lift and pitching moment coefficients than the RN. Moreover, variations in the infill profiles based on the RN have little effect on axial thrust but significantly affect the lift and pitching moment, improving the design flexibility when considering integrated vehicle requirements.

(3) As the tracing radius increases, the lift coefficient of both RN and CN decreases noticeably, while the axial thrust and pitching moment change only slightly. These findings provide useful guidance for future nozzle designs that aim to balance lift generation and moment matching.

Acknowledgements. The authors gratefully acknowledge the financial supports by the funding project STS/MY-ZY-2020–005 provided from science and technology on Scramjet laboratory of CARDC in China.

References

[1] Tsien, H.S. Similarity laws of hypersonic flow, *J. Math. Phys.*, 1946, **25**, pp 247–251.
[2] Edwards, C.L.W., Small, W.J., Weidner, J.P., et al. Studies of scramjet/airframe integration techniques for hypersonic aircraft, *AIAA*, 75–58.
[3] Lederer, R. and Kruger, W. Nozzle development as a key for hypersonics, *AIAA 93–5058*.
[4] Argrow, B.M. Comparison of minimum length nozzles, *J. Fluids Eng.*, 1998, **110**, (3), pp 283–288.
[5] Dumitrescu, L.Z. Minimum length axisymmetric Laval nozzles, *AIAA J.*, 1975, **13**, (4), pp 520–531.
[6] Zebbich, T. and Toubi, Z. Supersonic Two-Dimensional Minimum Length Nozzle Design at High Temperature, *AIAA Paper 2006–4599*.
[7] Goeing, M. Nozzle design optimization by method-of-characteristics, *AIAA 90–2024*.
[8] Hoffman, J.D. Design of compressed truncated perfect nozzles, *AIAA 85–1172*.
[9] Quan, Z.B., Xu, J.L. and Mo, J.W. Design of nonlinearly compressed SERN profile. *J. Propuls. Technol.*, 2012, **33**, (6), pp 951–955 (in Chinese).
[10] Zhao, Q., Xu, J.L. and Fan, Z.P.. Experimental and numerical study of truncation method for thrust nozzle profile based on balance of thrust and friction, *J. Propuls. Technol.*, 2014, **35**, (2), pp 151–156 (in Chinese).
[11] Östlund, J. *Flow Processes in Rocket Engine Nozzles with Focus on Flow Separation and Side-Loads*. Stockholm: Royal Institute of Technology Department of Mechanics, 2002.
[12] Rao, G.V.R. Exhaust nozzle contour for optimum thrust, *J. Jet Propuls.*, 1958, **28**, (3), pp 377–382.
[13] Lv, Z., XU, J.L., Yu, Y., et al. A new design method of single expansion ramp nozzles under geometric constraints for scramjets, *Aerosp. Sci. Tech.*, 2017, **66**, (7), pp 129–139.
[14] Yu, K.K., Xu, J.L., Lv, Z., et al. Inverse design methodology on a single expansion ramp nozzle for scramjets, *Aerosp. Sci. Tech.*, 2019, **92**, 9–19.
[15] Yu, K.K., Chen, Y.L., Huang, S., et al. Inverse design method on scramjet nozzles based on maximum thrust theory, *Aerosp. Sci. Tech.*, 2020, **166**, pp 162–171.
[16] Chen, Y.L., Yu, K.K. and Xu, J.L. A new design method on scramjet nozzles with strong geometric constraints, *Acta Aeronaut. Astronaut. Sin.*, 2021, **42**, (6), pp 253–263 (in Chinese).
[17] Lv, Z. and Xu, J.L. Design method for scramjet nozzles under geometric constraints, *J. Spacecr. Rockets*, 2022, **59**, (3), pp 806–815.
[18] Li, R., Xu, J.L., Yu, K.K., et al. Design and analysis of the scramjet nozzle with contact discontinuity, *Aerosp. Sci. Tech.*, 2021, **113**, pp 106695.
[19] Walker, S., Tang, M., Morris, S., et al. Falcon HTV-3X – A reusable hypersonic test bed. AIAA Journal, 2008–2544.
[20] Thompson, H.D. and Murthy S.N.B. Design of optimized three-dimensional nozzles. *J. Spacecr.*, 1966, **3**, (9), pp 1384–1393.
[21] Snyder, L.E. and Thompson, H.D. Three-dimension thrust nozzle design for maximum axial thrust, *AIAA J.*, 1971, **9**, (10), pp 1891–1892.
[22] Tanimizu, K., Mee, D.J., Stalker, R.J., et al. Nozzle design study for a quasi-axisymmetric scramjet-powered vehicle at Mach 7.9 flight conditions, *Shock Waves*, 2013, **23**, pp 453–460.
[23] Billig, F.S. and Kothari, A.P. Streamline tracing: technique for design hypersonic vehicles, *J. Propels. Power*, 2000, **16**, (3), pp 465–471.

https://doi.org/10.1017/aer.2026.10153 Published online by Cambridge University Press

[24] Taylor, T.M. and Vanwie, D. Performance Analysis of hypersonic shape-changing inlets derived from morphing streamline traced flowpath, *AIAA Paper 2008–2623*.
[25] Lu, X., Yue, L.J., Xiao, Y.B., et al. Design of scramjet nozzle employing streamline tracing technique, *AIAA 2009–7248*.
[26] Mo, J.W., Xu, J.L., Gu, R., et al. Design of an asymmetric scramjet nozzle with circular to rectangular shape transition, *J. Propuls. Power*, 2014, **30**, (3), pp 812–819.
[27] Lv, Z., Xu, J.L. and Mo, J.W. Design and analysis on three-dimensional scramjet nozzles with shape transition, *Aerosp. Sci. Tech.*, 2017, **71**, (12), pp 189–200.
[28] Hua, W.D. and Xu, J.L. Design approach and experiment of three-dimensional over/under TBCC exhaust system, *J. Aerosp. Power*, 2018, **33**, (9), pp 2268–2277 (in Chinese).
[29] Kunze, J., Smart, M.K. and Gollan, R. A design method for three-dimensional scramjet nozzles with shape transition, *J. Propuls. Power.* 2022, **38**, (1), pp 3–17.
[30] Armstrong, W.C. A method of characteristics computer program for three-dimensional supersonic internal flows, Arnold Engineering Development Center, Engine Test Facility, Air Force Systems Command, United States Air Force, 1979.
[31] Wdtanahc, S. A scramjet nozzle experiment with hypersonic external flow, *AIAA 92-3289*.

Cite this article: Zhang Z., Song W. and Zhou Z. (2026). A design method for single expansion ramp nozzle based on three-dimensional characteristic method. *The Aeronautical Journal*, **130**, 1836–1858. https://doi.org/10.1017/aer.2026.10153

https://doi.org/10.1017/aer.2026.10153 Published online by Cambridge University Press